Journal of Alloys and Compounds 900 (2022) 163488

Contents lists available at ScienceDirect

Journal of Alloys and Compounds

journal homepage: www.elsevier.com/locate/jalcom

Corrosion behavior of age hardening aluminum alloys produced by high-energy ball milling

Furkan Ozdemir[a,b], Chathuranga Sandamal Witharamage[a], Ahmed Abdelazim Darwish[a], Hasan Okuyucu[b], Rajeev Kumar Gupta[a,*]

[a] Department of Materials Science and Engineering, North Carolina State University, Raleigh, NC 27695, USA
[b] Department of Materials Engineering, Ankara Yildirim Beyazit University, Ankara, Turkey

ARTICLE INFO

Article history:
Received 20 June 2021
Received in revised form 16 November 2021
Accepted 26 December 2021
Available online 29 December 2021

Keywords:
High-energy ball milling
Aluminum alloys
Nanocrystalline alloys
Age hardening
Pitting corrosion

ABSTRACT

The influence of high energy-ball milling (HEBM) on corrosion and hardness of age hardening aluminum alloys was investigated. Nanocrystalline age hardening (AA2024, AA6061 and AA7075) alloys were produced by HEBM of pre-alloyed powder and subsequent cold compaction under uniaxial pressure of 3 GPa. Cyclic potentiodynamic polarization and immersion tests were conducted in 0.6 M NaCl solution which revealed significantly increased pitting and protection potentials in the HEBM alloys compared to wrought alloys of same composition. X-ray diffraction analysis and transmission electron microscopy indicated grain refinement below 100 nm in the ball milled alloys which was the major strengthening mechanism in the age hardening HEBM alloys. The superior corrosion resistance and hardness of the age hardening ball milled alloys were attributed to nanocrystalline structure, extended solid solubility and homogenous microstructure- free from coarse intermetallic phases.

1. Introduction

Aluminum is an active metal and yet corrosion resistant in the pure form due to presence of a protective oxide film (alumina) on the surface [1]. However, most of aluminum alloys exhibit poor corrosion performance owing to the microstructural heterogonies which lead to micro-galvanic interaction [2]. 2xxx, 6xxx and 7xxx series of commercial aluminum alloys are strengthened by age hardening where the strength and corrosion performance depends upon the composition, crystal structure, size, shape, and distribution of the precipitates [3–5]. The complex microstructures in age hardening alloys incorporate secondary phases comprising of Cu, Zn, Mg, Si as primary alloying elements and Fe, Cr, Ti, Mn as impurities or secondary additives [6]. Secondary phases in aluminum alloys are classified into three main categories; constituent particles, precipitates and dispersoids, which develop during solidification and thermomechanical treatment to obtain desired mechanical properties [6,7]. The effects of secondary phases on the localized corrosion in age hardening aluminum alloys have been widely reported [3,7–13].

Localized corrosion in the age hardening aluminum alloys depends on chemical composition, size and spatial distribution of the secondary phases occurred during metal forming and subsequent thermo-mechanical processing. Electrochemical nature of the secondary phases, depending on the composition, could be anodic or cathodic with respect to the matrix. Relatively noble particles like Al_2Cu, AlFeMnSi, AlCuFeSi, AlCuFeMn can act as local cathodes that cause the dissolution of adjacent matrix leading to the pitting corrosion [8,9,11,14–23]. Active particles like $MgZn_2$, Mg_2Al_3 and Mg_2Si act as local anodes that cause self-dissolution and forms pits [8,9,11,14–23]. Localized corrosion as well as formation of secondary phases depend upon the initial microstructure, including grain size of the alloys. Physical breakdown of secondary phases and increased passivation ability via grain refinement is attributed to enhanced corrosion resistance [24,71]. On contrary, some studies claim an inverse relationship with grain refinement and corrosion resistance [25]. Microstructure and therefore corrosion of an alloy is highly dependent on the production and post-production processes. Approximately 75–80% of the total aluminum products are comprised of wrought aluminum alloys which are produced from homogenized cast ingots via forging, rolling or extrusion where the secondary phases are broken and dispersed within the alloy during the metal forming processes [1,26]. Moreover, the characteristics of the phases formed during age hardening treatment in the age hardenable alloys dictate the hardness and corrosion resistance [27,28].

* Corresponding author.
E-mail address: rkgupta2@ncsu.edu (R.K. Gupta).

https://doi.org/10.1016/j.jallcom.2021.163488
0925-8388/

Table 1
Composition of the alloys used herein. Composition of the commercial alloys (AA2024-T3, AA6061-T6, AA7075-T6) was provided by the supplier (McMaster Carr). Composition of the as received alloy powder (AA2024, AA6061, and AA7075) was provided bu the supplier (Valimet). Composition of the ball milled and subsequently cold compacted alloys (HEBM-2024, HEBM-6061, and HEBM-7075) was determined using EDS area maps.

Alloy	Concentration (wt%)								
	Al	Cu	Mg	Mn	Fe	Si	Cr	Ti	Zn
AA2024-T3	Bal.	3.8–4.9	1.2–1.8	0.3–0.9	0–0.5	0–0.5	0–0.1	0–0.15	0–0.25
AA6061-T6	Bal.	0.05–0.4	0.8–1.2	0–0.15	0–0.7	0.4–0.8	0.4–0.8	0.0.15	0–0.25
AA7075-T6	Bal.	1.2–2	2.1–2.9	0–0.3	0–0.5	0–0.4	0.18–0.29	0–0.2	5.1–6.1
AA2024	Bal.	3.8–4.9	1.2–1.8	0.3–0.9	0.5 Max	0.5 Max	0.1 Max.	0.15 Max	0.25 Max
AA6061	Bal.	0.15–0.4	0.8–1.2	0.15 Max.	0.7 Max	0.4–0.8	0.04–0.35	0.15 Max	0.25 Max
AA7075	Bal.	1.2–2.0	2.1–2.9	0.30 Max	0.5 Max	0.4 Max	0.18–0.28	0.20 Max	5.1–6.1
HEBM-2024	Bal.	4.35	1.61	0.30	0.36	0.30	0.1	0.1	–
HEBM-6061	Bal.	0.41	1.20	0.15	0.65	0.82	0.25	0.1	–
HEBM-7075	Bal.	1.85	2.84	0.2	0.45	0.22	0.2	0.1	5.78

The methods providing modified microstructures such as melt spinning, ion implantation, sputter deposition, electrodeposition and mechanical alloying are elicited the remarkable modifications in the mechanical performance and localized corrosion resistance in metastable alloys. [29]. Recent literature on Al-Mg alloys showed improvement in the mechanical performance by severe plastic deformation, extrusion and additive manufacturing methods [72–76,79,80,81,82]. High-energy ball milling (HEBM) is a technique to impart high strength by grain refinement, uniform dispersion of fine ceramic particles and extended solid solubility [30,31]. HEBM in combination with suitable alloying elements has also been reported to corrosion performance of aluminum alloys and the underlying mechanisms are discussed in [29,32–34]. Coarse secondary phases are either dissolved or extensively refined during the HEBM [32,35–38,77,78]. Additionally, milling enhances diffusion of the alloying elements and defect concentrations which influences the precipitation [32,39]. Therefore, microstructural evolution and properties of the high-energy ball milled alloys during thermo-mechanical processing and in service are expected to be different than the commercial alloys of the same chemical composition. [32,40,41,77]. For example; modified grain boundary segregation of Mg in nanocrystalline Al-Mg alloys was observed [42,43]. Moreover, intergranular corrosion (IGC) and stress corrosion cracking (SCC) caused by the precipitation of intermetallic (Mg_2Al_3, when exposed to 50–200 °C in Al-Mg alloys with more than 3.5 wt% Mg) can be influenced by the increased diffusivity of Mg as a result of HEBM [32,44,45]. Furthermore, hydrogen embrittlement may also be influenced by the possible enhancement of H diffusivity in Al alloys [32].

Corrosion behavior of commercial Al alloys produced by HEBM of pre-alloyed powder is reported only in a few studies [37,38,46]. For examples, ball milled AA5083 has been reported to exhibit high corrosion resistance due to the refinement of intermetallics and grains, and possible incorporation of elements from milling media [37]. Furthermore, the corrosion behavior of age hardening alloys such as 2024, 6061 and 7075 produced by high energy ball milling is not reported in the literature. Therefore, investigation of the corrosion behavior of age hardening nanocrystalline Al alloys such a great merit. In the present study, the hardness and corrosion behavior of AA2024, AA6061 and AA7075 alloys produced by cold compaction posterior to HEBM of pre-alloyed powder have been investigated. The results were compared with commercially available wrought AA2024-T3, AA6061-T6 and AA7075-T6 alloys.

2. Materials and methods

Gas atomized powders (Commercially available from Valimet, −325 mesh) of AA2024, AA6061 and AA7075 were high energy ball milled in a planetary ball mill (Fritsch Pulverisette 5) for 100 h at a speed of 280 rpm. The ball to powder weight ratio was selected as 16:1 for 10 mm diameter stainless-steel balls. Stearic acid (1.5 wt%) was used as process controlling agent to avoid cold welding. The powder loading and sealing of the jars were done in a glove box with high purity argon atmosphere (O_2 < 50 ppm). The HEBM was interrupted for 1 h after each hour of milling to minimize the overheating. The obtained powders were consolidated under the load of 11840 kg on a 7 mm diameter tungsten carbide die encased in steel core. Consolidation was conducted in ambient laboratory temperature using a dwell time of 10 min for each sample. The alloys produced by HEBM and subsequent cold compaction have been termed as HEBM-2024, HEBM-6061, and HEBM-7075 in this study.

Wrought alloys were also investigated to compare the properties. 3 mm thick wrought alloy plates of AA2024-T3, AA6061-T6 and AA7075-T6 (McMaster-Carr) were procured and machined into 12 mm × 12 mm coupons. The chemical composition of the as received gas atomized powders, high-energy ball milled and cold compacted samples, and wrought alloys are presented in Table 1.

2.1. X-ray diffraction

The x-ray diffraction experiments were conducted in the Rigaku SmartLab equipped with graphite monochromator and Cu Kα radiation (λ = 0.154056 nm) with a step size of 0.01° at a scanning speed of 1°/min within the range of 25–85°. The mean crystallite size and lattice strain were calculated by Rietveld method [47,48] after determining the contribution of instrumental broadening using LaB6 standard.

2.2. Hardness test

Vickers hardness of the alloys was collected using a Wilson-Tukon hardness tester by applying of 50 g load for 10 s. The alloys were ground to 1200 grit SiC paper finish and ultrasonicated in ethanol. The hardness tests were repeated at least 10 times for each sample to calculate average Vickers hardness.

2.3. Electrochemical tests

Electrochemical tests were conducted using a conventional three-electrode flat-cell. Cyclic potentiodynamic polarization (CPP) were performed in 0.6 M NaCl. The copper tape was attached to back of the samples, which were cold mounted into epoxy resin. The samples were ground up to 1200 SiC grit under ethanol following 800, 600 and 400 under running water. The interface between the metal and epoxy was covered with quick set epoxy resin (Araldite) to

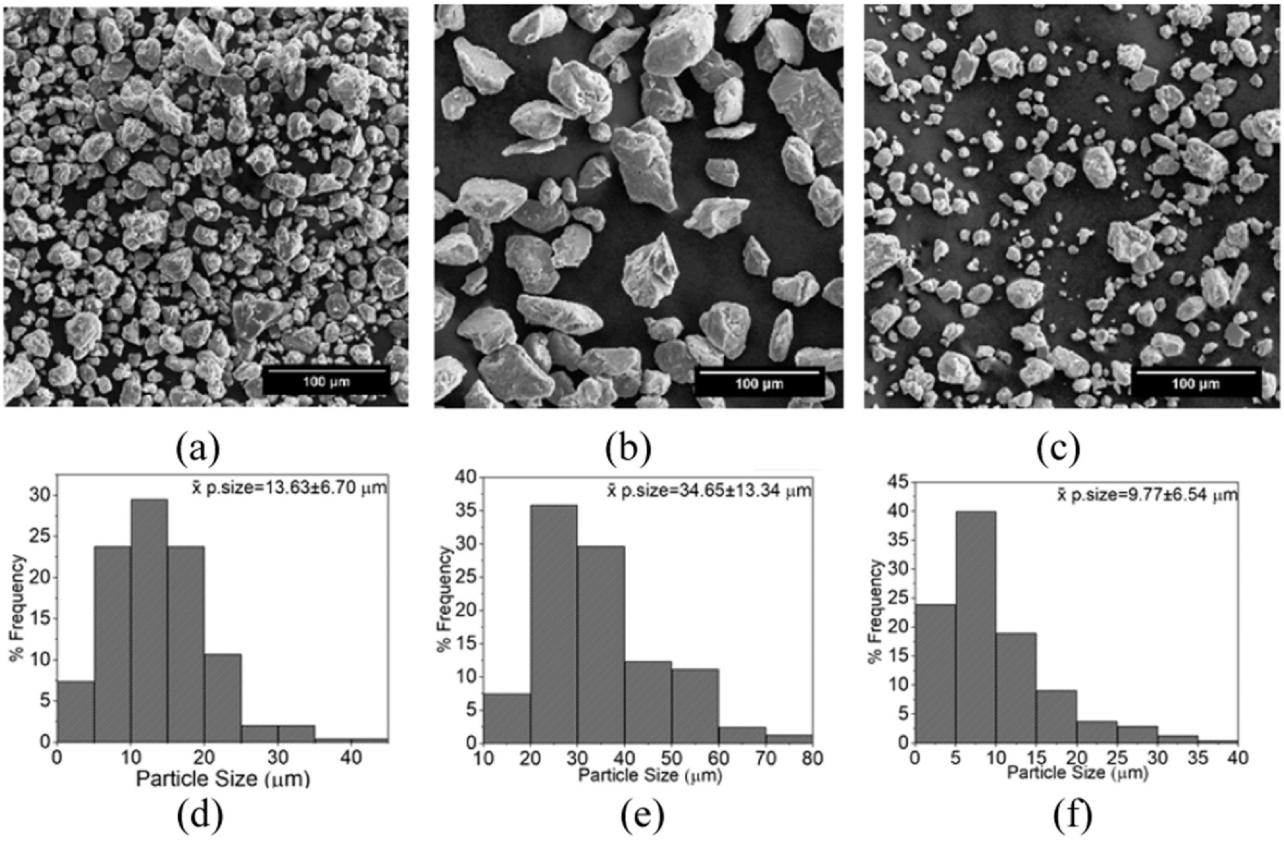

Fig. 1. Back scattered electron images for (a) HEBM-2024 powder, (b) HEBM-6061 powder, (c)HEBM-7075 powder. Distribution of the particle size for (d) HEBM-2024 powder, (e) HEBM-6061 powder, (f)HEBM-7075 powder.

avoid possible crevice corrosion. The samples were stored in a fume box for 24 h after application of epoxy.

A multichannel potentiostat (Biologic VMP-300) with EC-lab software was used for the electrochemical tests. Samples were the working electrodes. A platinum mesh was used as the counter electrode and the reference electrode was a saturated calomel electrode (SCE). The open circuit potential (OCP) was measured 0.5 h in order to obtain stabilized electrodes. The CPP curves were obtained with a scan rate 1 mV/s from 0.1 V_{SCE} below the corrosion potential (E_{corr}) until the current density reached 1 mA/cm^2 at which point the direction of scan was then reversed thereafter. Potentiostatic polarization curves were obtained by applying a constant anodic potential (150 mV above open current potential) in 0.6 M of NaCl solution. The potentiostatic polarization tests were initiated after stabilization of open circuit potential for 30 min.

2.4. Scanning electron microscopy (SEM) and transmission electron microscopy (TEM) characterization

Samples were brought to 0.05 µm surface finish using diamond suspension and cleaned in ultrasonic ethanol bath for 5 min before SEM analysis. The SEM studies were performed in a FEI Verios 460 L field emission SEM with an Oxford energy dispersive X-ray spectrometer (EDS) with an electron landing energy of 20 kV.

Specimen for TEM investigation was prepared in a ThermoFisher Quanta 3D FEG, a Focused Ion Beam and Scanning Electron Dual-beam Microscope (FIB-SEM). Specimen was protected with platinum deposition to avoid surface damage due to ion beam. 30 kV of landing voltage with different beam currents was utilized to monitor the specimen with minimum ion beam damage. In-situ lift-out of the cross section with an approximate thickness of 1–2 µm of lamella was carried out with an omniprobe manipulator. This lamella was placed on a TEM grid for further thinning and cleaning from Ga contamination. TEM specimen (HEBM-2024) was kept under vacuum after final polishing until TEM investigation for sub-surface morphology investigation in a Thermofisher Talos F200X Field Emission Gun Scanning Transmission Electron Microscope (S/TEM) operated at 200 kV.

3. Results and discussion

3.1. Microstructural characterization

Representative backscattered electron image (BSE) of the high energy ball milled powders of alloy 2024, 6061, 7075 and corresponding particle size distribution are shown in Fig. 1. The mean particle size of the HEBM-2024 powder, HEBM-6061 powder and HEBM-7075 powder was measured as 13.63 (± 6.7) µm, 34.65 (± 13.34) µm and 9.77 (± 6.54) µm respectively. The ball milled powder were produced by the HEBM of gas atomized powder. Gas atomization is the process of breaking molten metal with a high-speed inert gas stream that provides rapid solidification of the droplets. In aluminum alloys, shape of the gas atomized powder particles is primarily spherical [49]. The 320-mesh gas atomized powders were spherical prior to milling while high energy ball milled powders were more irregularly shaped. The irregularity in the size and variation in the particle size are of the alloys can be attributed to the repetitive welding, fracture and re-welding phenomenon during HEBM [50].

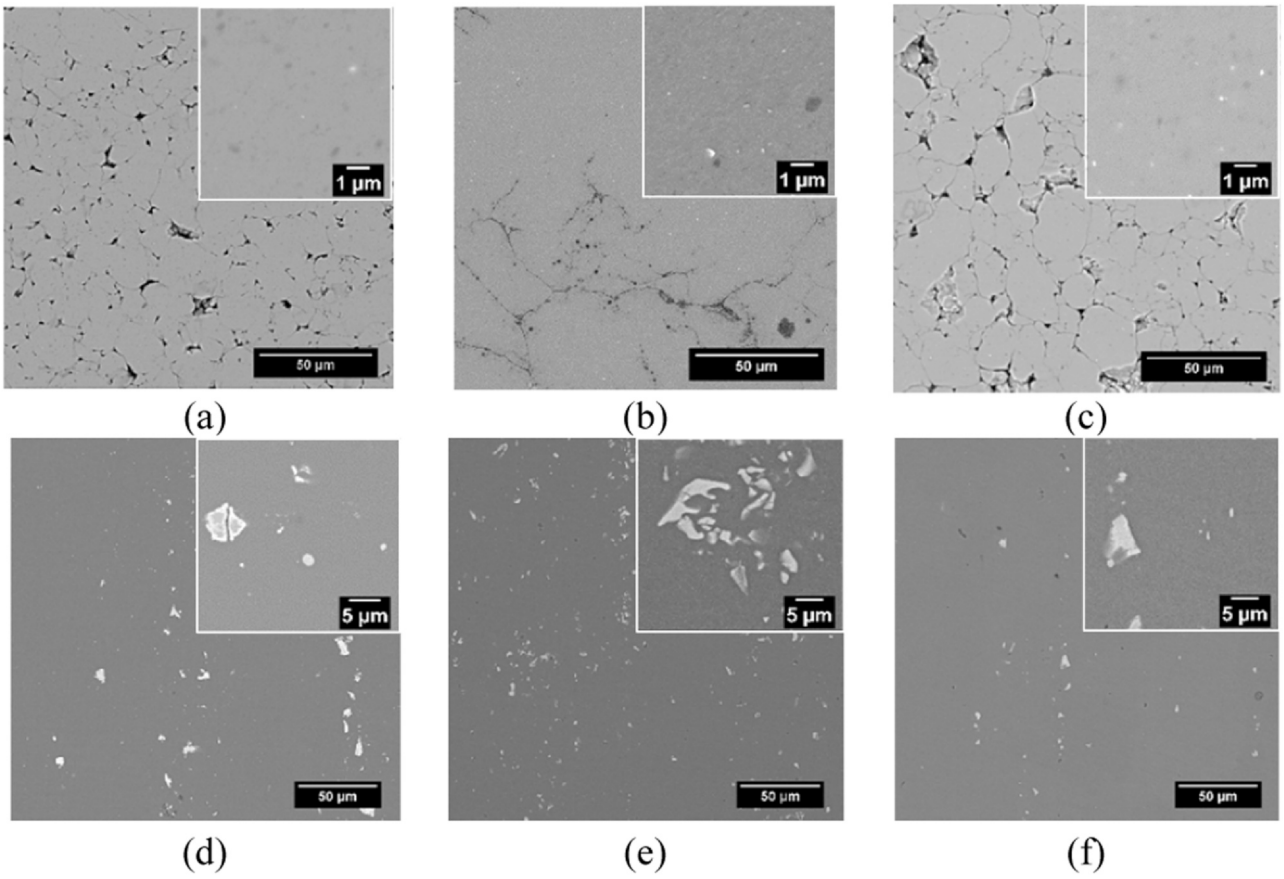

Fig. 2. Back scattered electron images for (a) HEBM-2024, (b) HEBM-6061, (c) HEBM-7075, (d) AA2024-T3, (e) AA6061-T6 and (f) AA7075-T6. Corresponding high magnification images are shown in the inset.

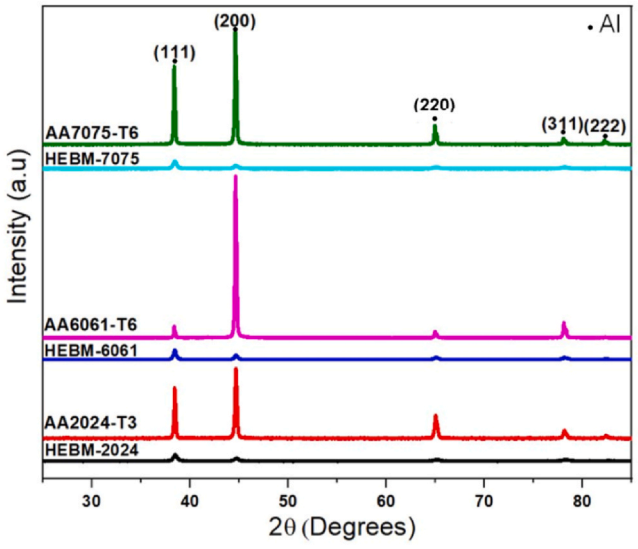

Fig. 3. XRD patterns of AA2024-T3, AA6061-T6, AA7075-T6 and HEBM-2024, HEBM-6061, HEBM-7075.

Fig. 2 shows the BSE images of the ball milled and subsequently consolidated alloys (HEBM-2024, HEBM-6061, HEBM-7075) and wrought alloys (AA2024-T3, AA6061-T6 and AA7075-T6). The HEBM alloys, presented in Fig. 2a-2c, indicated a homogenous microstructure, free from coarse intermetallics that were detected in the wrought alloys (Fig. 2d-2f). The microstructure of the HEBM alloys demonstrated porosity on the surface which is inherent to the cold compaction process and can be attributed to the highly hardened and irregularly shaped particles. Coarse intermetallic particles were observed in the wrought alloys and EDS analysis indicated presence of mainly Al_2CuMg and AlFeMnMg in AA2024-T3; Mg_2Si and AlFeSi in AA6061-T6, Mg_2Si and Al_7Cu_2Fe compounds in AA7075-T6. BSE images of HEBM alloys indicated matrix with uniformly distributed fine bright particles (below 200 nm) and dark particles (below 80 nm) in each case. EDS analysis indicated that the bright particles contain Fe and Cr, and therefore can be attributed to the abrasion of stainless steel which is the material of milling media. The dark particles could be considered as pores or oxides or nitrides that might be incorporated from the milling atmosphere or stearic acid which was used as process controlling agent (PCA). Use of PCA might not be very attractive for HEBM due to the possible decomposition and therefore contamination during the process [84]. However; characteristics of the ball milled powder such as the shape, size, purity, chemical and thermal stability are highly dependent to the type and amount of PCA [83].

X-ray diffraction (XRD) patterns for both HEBM and wrought alloys are presented in Fig. 3. XRD spectra of all alloys was mainly comprised of Al peaks. When compared to wrought alloys, all HEBM alloys demonstrated significant peak broadening which is the indicator of grain refinement. The peak broadening of the Al peaks (considering the contribution of instrumental broadening) was employed to calculate the grain size and lattice strain via Rietveld method [48]. The grain size of the HEBM-2024, HEBM-6061, HEBM-

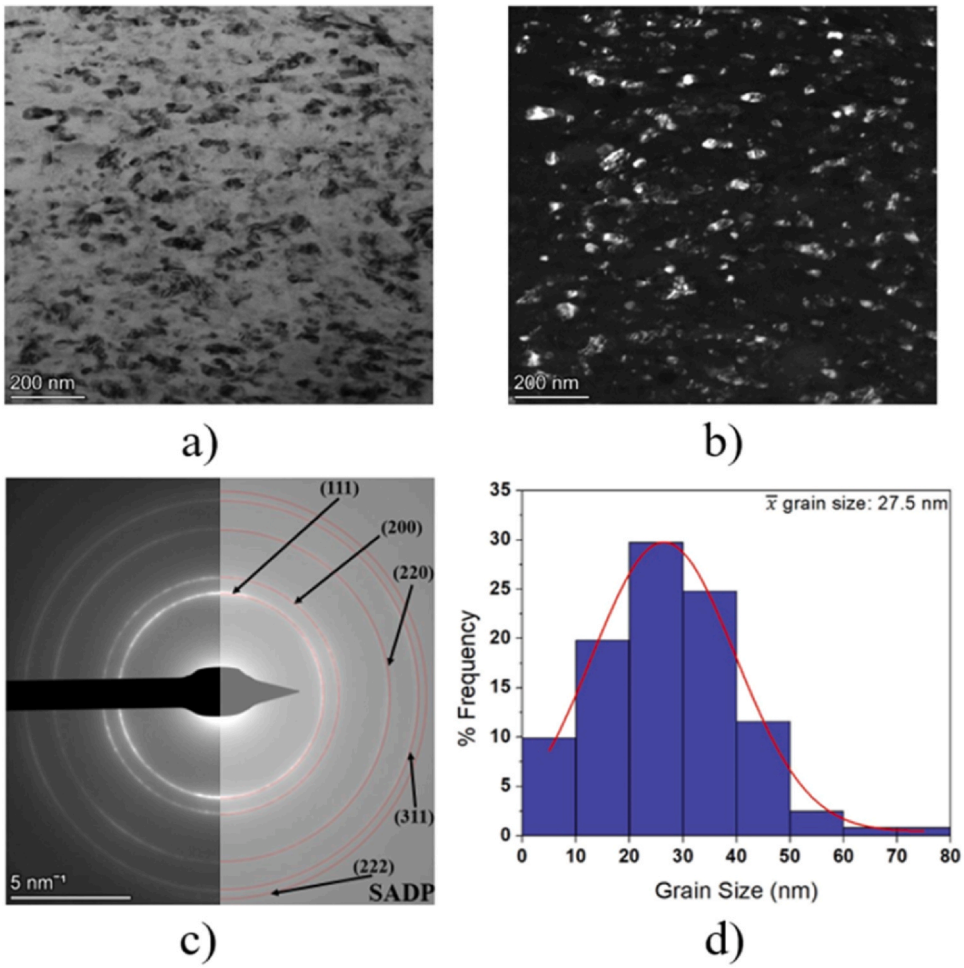

Fig. 4. TEM micrographs of HEBM-2024; a) BF image b) DF image c) SADP. d) Grain size and its distribution within the DF micrograph in b).

7075 were calculated respectively as 29 (±5) nm, 38 (±6) nm and 28 (±4) nm.

Fig. 4 shows TEM images of the HEBM-2024. The bright field (BF) and dark field (DF) images (Fig. 4a and 4b) show the existence of fine grains that further confirmed by the selected area diffraction pattern (SADP) presented in Fig. 4c. Comparison of SADP pattern with theoretical values obtained from Powder Diffraction File™ (PDF®) databases (PDF Card −00 to 004–0787_Al) revealed that the pattern belongs to Al-FCC with approximate lattice parameter of 4.07013 ± 0.00426 Å [85]. The grain size and its distribution within the DF image in Fig. 4b is presented in Fig. 4d. The average grain size for HEBM-2024 was determined as 27.5 (± 12.5) nm which are in close agreement with the grain size calculated via XRD analysis.

3.2. Corrosion behavior of the alloys

The cyclic potentiodynamic polarization (CPP) curves for HEBM-2024, HEBM-6061, HEBM-7075 along with AA2024-T3, AA6061-T6, AA7075-T6 are presented in Fig. 5. Polarization curves demonstrate the influence of HEBM on the corrosion behavior. The corrosion potential (E_{corr}), corrosion current density (i_{corr}), pitting potential (E_{pit}) and protection potential (E_{prot}) were determined from the CPP graphs and are presented in Table 2. The wrought alloys demonstrated no clear breakdown potential in the anodic branch which has been reported in the literature due to the occurrence of the pitting below the open current potential (OCP) [3,51,52]. A clear passive region was visible in the CPP curves for the ball milled alloys. Curves show absence of metastable pitting and evidence of passivity breakdown (pitting potential). Anodic polarization produces an increase in measured current density with increasing potential, as alloys are oxidized and ions transport through the oxide. The increase seems to be relatively comparable between the three experimental alloys, suggesting oxide films of similar thickness and/or growth rate during anodic polarization. The pitting potential of the ball milled alloys were significantly more positive than open current potential. HEBM alloys exhibited a wide passive window (E_{corr}-E_{pit}) whereas no passive window was visible for the wrought alloys. E_{corr} of the HEBM alloys were lower than the wrought alloys and this phenomenon can be attributed to the lower cathodic current density caused by the refined intermetallics. i_{corr} which is also calculated by Tafel extrapolation method indicated that i_{corr} of the HEBM alloys significantly lower than the wrought alloys. In addition, HEBM alloys indicated pit transition potential (E_{ptp}) and protection potential (E_{prot}) in all cases that the combination of all contributions can be interpreted as HEBM alloys have superior corrosion resistance among the investigated alloys.

Fig. 6 shows the current density versus time graph for the wrought and ball milled alloys in 0.6 M NaCl. The applied potential was 150 mV above the open circuit potential. The ball milled alloys shows a continuous decrease in the current density and currents reached < 1 μA/cm^2 which shows strongly passive nature of the alloys. On contrary, wrought alloys showed high current density,

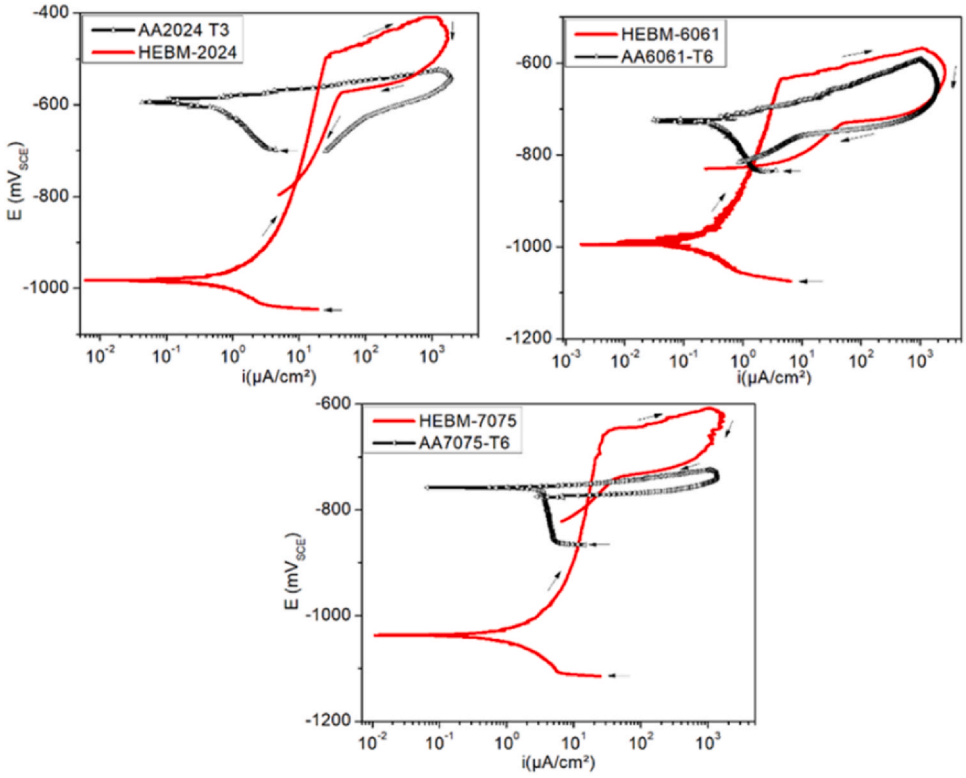

Fig. 5. Cyclic Potentiodynamic Polarization results of a-) HEBM-2024 and AA2024-T3, b-) HEBM-6061 and AA6061-T6, c-) HEBM-7075 and AA7075-T6.

exceeding 1 mA/cm2 in a few minutes (Fig. 6). Current density versus time graphs (Fig. 6) corroborated the conclusions from the CPP data (Fig. 5).

Fig. 7 indicates areas of the specimens that immersed in the 0.6 M NaCl solution for 1 h. It is observed that the corrosion in the wrought alloys was associated primarily with the constituent particles in the sample surface (Fig. 7d-7f). The BSE image indicated that the pitting that formed as trenches and dissolution of the intermetallic particles on the sample surfaces. EDS analysis verified that the secondary phase particles had galvanic interaction with the matrix. Al, Cu, Fe, and Mn containing particles were found to initiate the dissolution of matrix by leaving trenches at their surroundings. The dissolved particles were found Cu enriched (Fig. 7d and 7f), and Fe and Si enriched in Fig. 7e. The BSE images of HEBM-2024, HEBM-6061 and HEBM-7075 immersed for 1 h in 0.6 M NaCl are shown in (Fig. 7a-7c). The homogenous microstructure due to the refined or dissolved secondary phase particles led significant decrease in the size and number of pits observed in HEBM alloys. The EDS analysis indicated the particles responsible for the corrosion initiation as trenches in HEBM alloys contained Fe and Cr which are originated due to abrasion of milling media. Fig. 8 shows the morphology of alloys after immersion in 0.6 M NaCl for 14 days and subsequent removal of the corrosion products in 30 vol%. of HNO_3. The effects of prolonged immersion were apparently revealed in wrought alloys (Fig. 8d-8f). The BSE images indicated significantly larger pits that primarily associated to the dealloying of the constituent particles. The BSE images of HEBM-2024, HEBM-6061 and HEBM-7075 are presented in Fig. 8a-8c. The lack of coarse constituent particles and homogenous microstructures led sustainability of superior corrosion performance in the high-energy ball milled alloys.

3.3. Hardness of the ball milled alloys

Average Vickers microhardness of HEBM alloys and wrought alloys are presented in Fig. 9. Average Vickers hardness values were ~240 HV, ~185 HV and ~269 HV for HEBM-2024, HEBM-6061 and HEBM-7075 while the values for wrought AA2024-T3, AA6061-T6 and AA7075-T6 were ~137 HV, ~108 HV and ~176 HV. HEBM alloys indicated a significant increase in the hardness values which is consistent to the reported literature on the nanocrystalline aluminum alloys [35,37,53,54]. The high strength of the HEBM alloys was attributed to the joint influence of grain refinement, solid

Table 2
The average electrochemical parameters and corresponding standard deviations of alloys determined from CPP curves in 0.6 M NaCl at room temperature.

	E_{corr}	i_{corr}	E_{pit}	E_{ptp}	E_{prot}
	(mV_{SCE})	($\mu A/cm^2$)	(mV_{SCE})	(mV_{SCE})	(mV_{SCE})
HEBM-2024	-984 (± 82)	0.14 (± 0.06)	-477 (± 20)	-572 (± 6)	-736 (± 10)
AA2024-T3	-585 (± 23)	0.38 (± 0.02)	< E_{corr}	-627 (± 8)	–
HEBM-6061	-990 (± 133)	0.06 (± 0.02)	-623 (± 18)	-730 (± 8)	-824 (± 12)
AA 6061-T6	-722 (± 85)	0.22 (± 0.08)	-710 (± 19)	-755 (± 3)	–
HEBM-7075	-1035 (± 76)	0.15 (± 0.08)	-654 (± 12)	-738 (± 2)	-789 (± 13)
AA7075-T6	-757 (± 43)	3.36 (± 0.32)	< E_{corr}	–	–

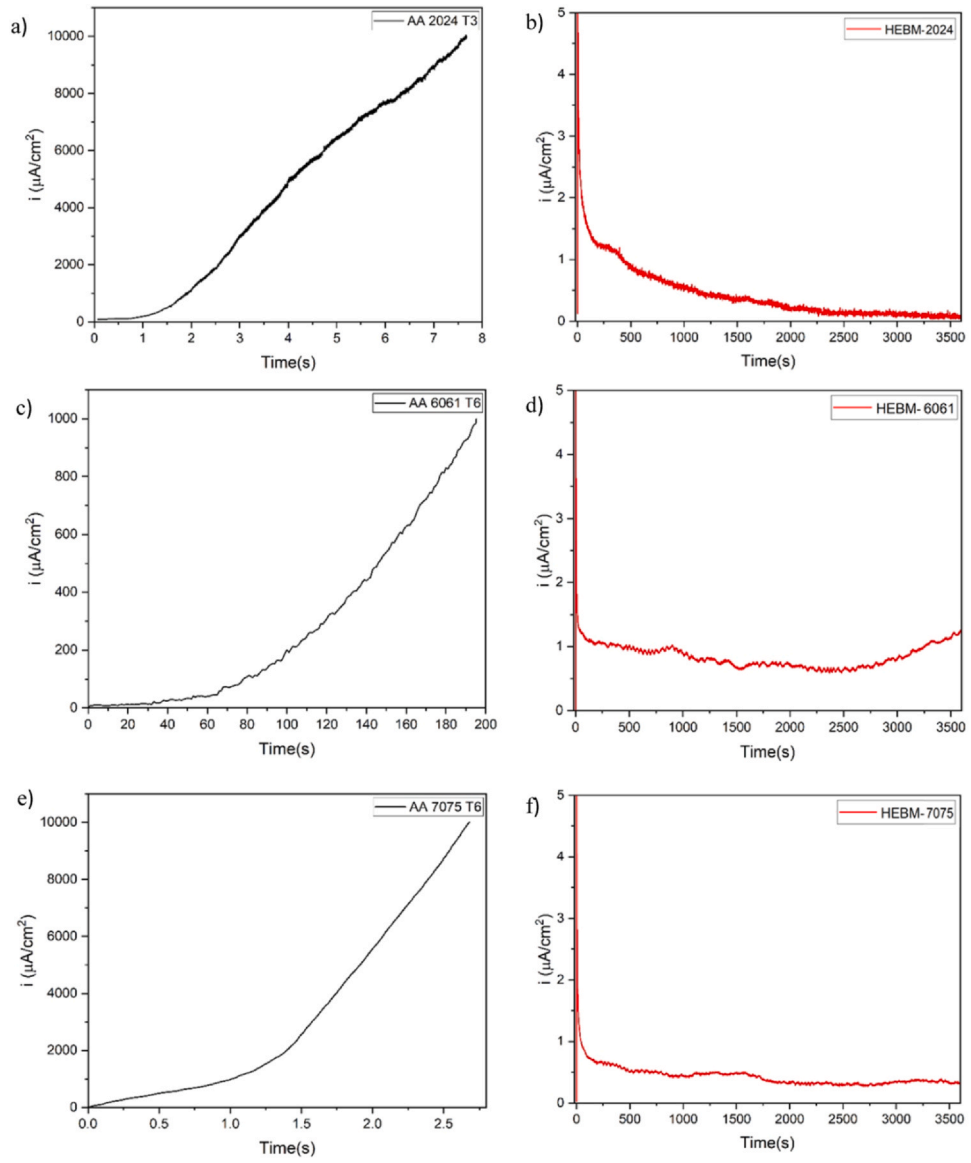

Fig. 6. Potentiostatic polarization 150 mV above open circuit potential after 30 min of stabilization in 0.6 M NaCl a) AA 2024 T3, b) HEBM-AA 2024, c) AA 6061 T6, d) HEBM-AA 6061, e) AA 7075 T6 and, b) HEBM-AA 7075.

solution strengthening and uniform dispersion of fine intermetallics [55]. The individual elements of the various strengthening mechanisms were quantified in several studies that reviewed in [55].

The total yield strength of the alloy can be quantified as:

$$\sigma_y = \sigma_o + \sigma_{gb} + \sigma_d + \sigma_{ss} + \sigma_{pp} \quad (1)$$

where, σ_o is the yield strength of base metal (17 MPa) [56]. σ_{gb} is the strength contribution by grain boundaries, σ_d is the yield strength contribution by dislocations, σ_{ss} is the yield strength contribution by solute atoms and σ_{pp} is the yield strength contribution by precipitates.

The yield strength of the HEBM alloys were predicted by Tabor's rule to estimate individual strength contributions.

$$\sigma_y \approx H^* \frac{1}{3} \quad (2)$$

Where H is the microhardness value in MPa. The estimated yield strength of the alloys were calculated as 784.56 MPa, 604.64 MPa and 879.36 MPa for HEBM-2024, HEBM-6061 and HEBM-7075 respectively.

The estimation of the strength contribution by grain boundaries (σ_{gb}) were calculated by the Hall-Petch equation [56]:

$$\sigma_{gb} \approx k(d)^{1/2} \quad (3)$$

where, k is the Hall-Petch coefficient 0.09 $MPa^{1/2}$ [35,57,58] and d is the grain size. The estimated contributions of σ_{gb} were calculated for 528.49 MPa, 455.7 MPa and 569.20 MPa for HEBM-2024, HEBM-6061 and HEBM-7075 respectively. Calculations indicated that the major contribution to the yield strength was by grain boundaries.

The contribution of dislocation strengthening (σ_d) is obtained by Bailey-Hirsch equation [59,60]:

$$\sigma_d = \underline{M}\alpha G b \rho^{\frac{1}{2}} \quad (4)$$

Where $\underline{M}$ is average orientation factor (3.06), α is constant (0.2), G is shear modulus (26 GPa), b is burger's vector (0.286 nm) and ρ is the dislocation density that calculated by:

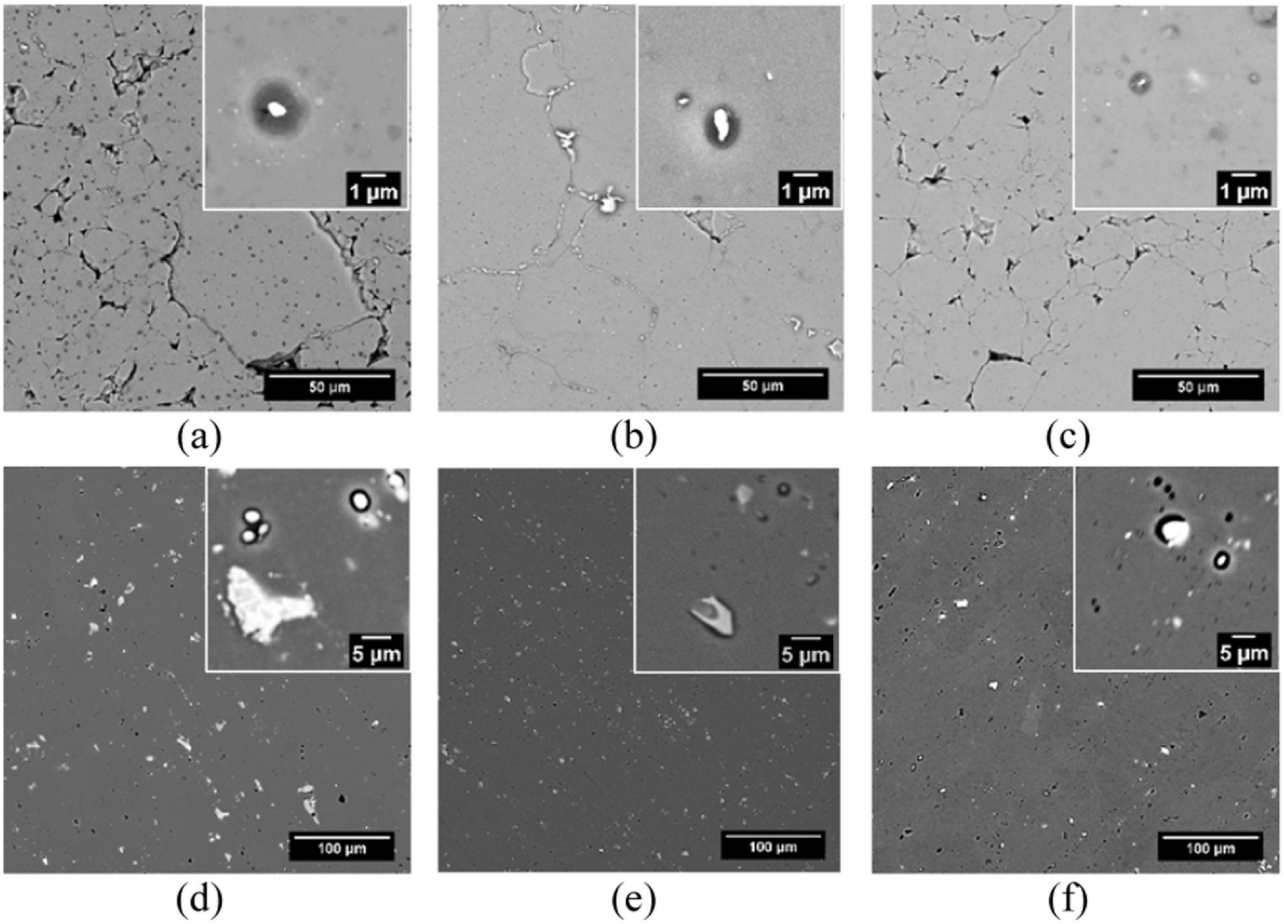

Fig. 7. SEM micrographs after 1 h of immersion in 0.6 M NaCl (a) HEBM-2024, (b) HEBM-6061, (c) HEBM-7075, (d) AA2024-T3, (b) AA6061-T6 and (c) AA7075-T6 without removing the corrosion products. Corresponding high magnification images are shown in the inset.

$$\rho = \frac{2\sqrt{3}\,\varepsilon}{Db} \tag{5}$$

Where ε is lattice strain and D is grain size that are calculated from XRD data.

The increment in the strength caused by dislocation strengthening was calculated as 165.96 MPa, 119.36 MPa and 170.33 MPa for HEBM-2024, HEBM-6061 and HEBM-7075 respectively. Calculations indicated that the dislocation strengthening was secondary contribution in HEBM alloys after strength contribution by grain boundaries.

The strength contribution by solute atoms (σ_{ss}) were calculated by following equation [59,61]:

$$\sigma_{ss} = \underline{M}Gb\varepsilon^{\frac{3}{2}}c^{\frac{1}{2}} \tag{6}$$

where c is the solute concentration with the power that assumed as 0.5 [59]. Solute contribution is dependent to the lattice strain which arises from the difference between solute and solvent atom size. Table 3 shows primary solute atoms in the commercial aluminum alloys and theoretical contributions to yield strengths using the data on high-purity binary alloys [2]. Assuming complete solubility of all solute atoms with the HEBM process would enable to calculate maximum theoretical contribution by solute solution strengthening. Therefore, maximum theoretical contribution of σ_{ss} was calculated as 102.56 MPa, 39.75 MPa and 103.5 MPa for HEBM-2024, HEBM-6061 and HEBM-7075 respectively. Considering the theoretical maximum as free of possible secondary phases that consist of the compounds of solutes are not dissolved in the solvent, the actual contribution values must be less and thus it can be concluded that the contribution of the solute atoms to strengthening was not significant.

Experimental value of yield strength (calculated by Tabor's rule) and calculated individual contributions of grain boundary strengthening, solid solution strengthening and dislocation strengthening to the estimated theoretical yield strength are shown in Fig. 10. Grain refinement contribution was in between 65% and 74% of the total estimated strength of the HEBM alloys. Therefore, grain refinement could be agnominated as dominant mechanism in the enhanced strength. Contribution by precipitates and dispersoids can be estimated by Orowan strengthening (σ_{Or}) [58] which is dependent to radius of the precipitates. SEM analysis did not provide enough data about the size and shape of precipitates in HEBM alloys. However, σ_{Or} were reported to have minor contributions in the high-energy ball milled alloys despite the Orowan strengthening has accountable contribution in precipitation hardened alloys [57,62–64].

4. General discussion

Constituent particles which include active alloying elements found in the investigated wrought alloys were highly associated to localized corrosion. AA2024-T3 indicated a high Al_2CuMg content which was reversed from more noble to less-noble particles by dealloying and incongruent dissolution when exposed to 0.6 M NaCl solution [7]. Corrosion is mainly attributed to S-phase particles together with Fe containing particles which were responsible for the

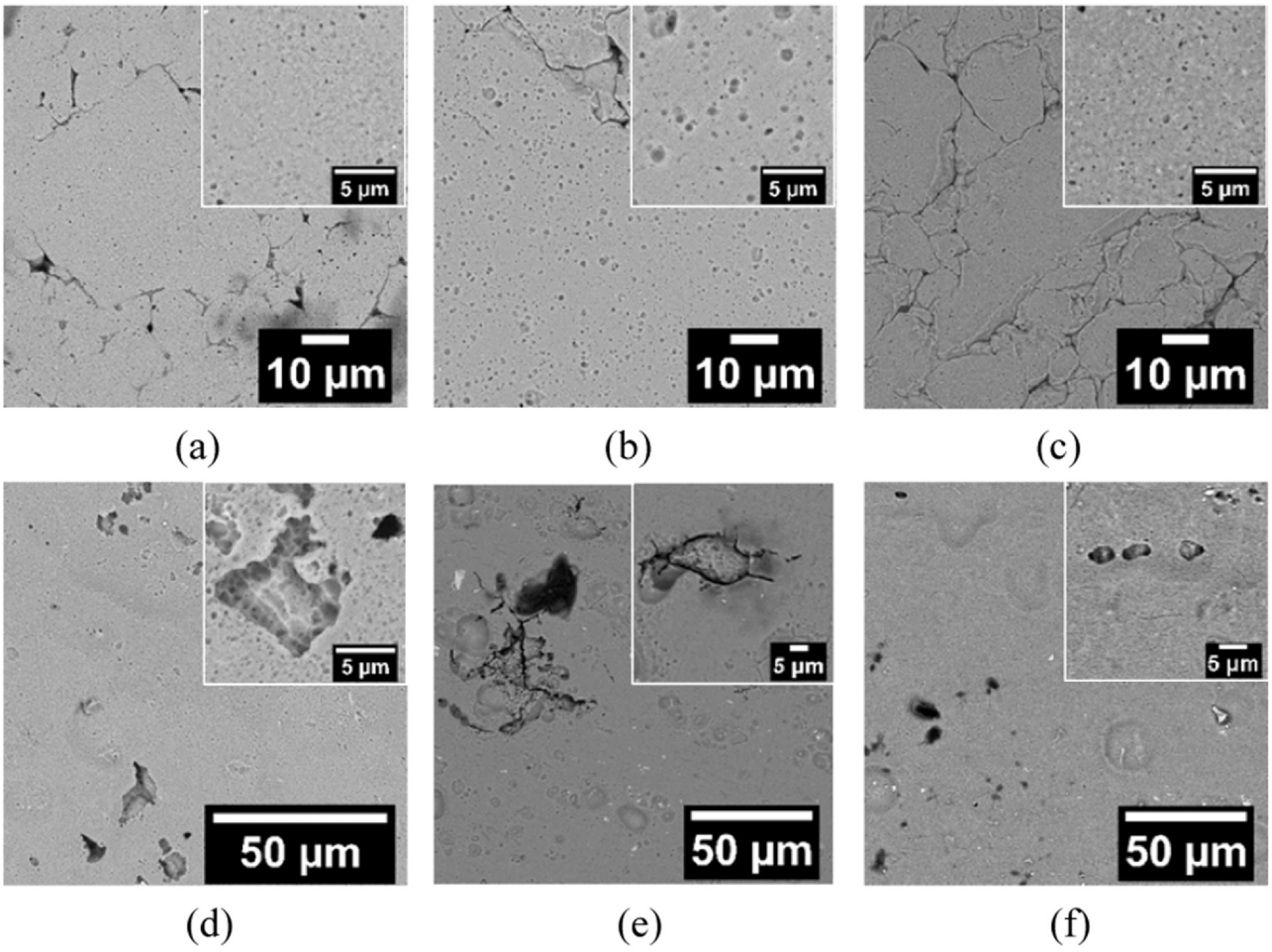

Fig. 8. SEM micrographs after 14 days of immersion in 0.6 M NaCl (a) HEBM-2024, (b) HEBM-6061, (c) HEBM-7075, (d) AA2024-T3, (e) AA6061-T6 and (f) AA7075-T6 after removing the corrosion products. Corresponding high magnification images are shown in the inset.

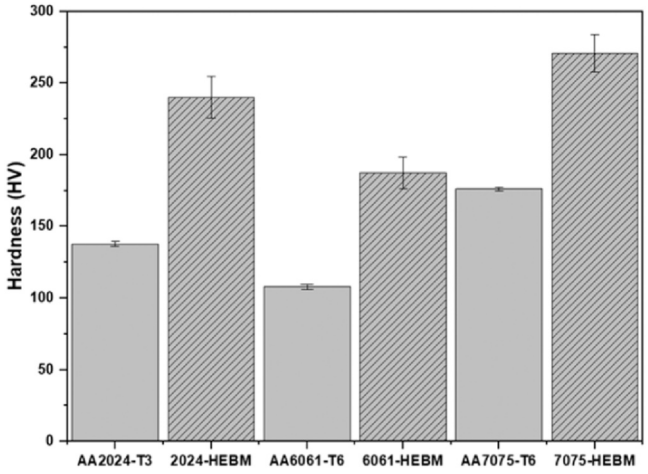

Fig. 9. Vickers hardness measured for AA2024-T3, AA6061-T6, AA7075-T6 and HEBM-2024, HEBM-6061, HEBM-7075.

dissolution of matrix of 2024-T3 [9,21,52,65,66]. In addition to Cu containing phases, Zn containing particles such as $MgZn_2$ were mainly attributed to the anodic dissolution or peripheral pitting depending on the electrochemical activity of the secondary phase respect to the matrix in AA7075-T6 [7]. Al-Si-Fe-containing cathodic particles and Mg_2Si could be attributed to the matrix dissolution in AA6061-T6 [67].

Corrosion behavior of the aluminum alloys mainly associated to characteristics of secondary phase particles and their interaction with the matrix. The modification in the corrosion behavior of HEBM alloys could be attributed to the HEBM process which is known to provide nanocrystalline structures with enhanced diffusivity and free energy, formation of super saturated matrix and metastable phases, and increased homogeneity in the microstructure [37,38,54,68,69]. Furthermore, significant refinement of Fe and Cu rich intermetallics by the HEBM process (seen in Fig. 2) is expected to decrease the cathodic sites and therefore overall cathodic reaction rate which is oxygen reduction reaction for the corrosion of aluminum alloys [70]. A decrease in the cathodic reaction due to refined microstructure could be attributed to high corrosion resistance in the ball milled alloys.

This study indicated that hardness and corrosion performance of the age hardening commercial alloys could be significantly enhanced by the high-energy ball milling. The powder obtained by high energy ball milling is a promising feedstock material for possible applications of several additive manufacturing and surface modification techniques.

Table 3
Primary solute atoms in HEBM alloys and their contribution to yield strength.

Element	Yield Strength addition (MPa wt%$^{-1}$)[2]	Concentration (wt%)			Yield Strength Contribution (MPa)		
		2024	6061	7075	2024	6061	7075
Si	9.2	0.3	0.8	0.2	2.76	7.36	1.84
Zn	2.9	–	–	5.8	–	–	16.82
Cu	13.8	4.35	0.4	1.8	60.03	5.52	24.84
Mn	30.3	0.3	0.15	0.2	9.09	4.54	6.06
Mg	18.6	1.6	1.2	2.9	29.76	22.32	53.94

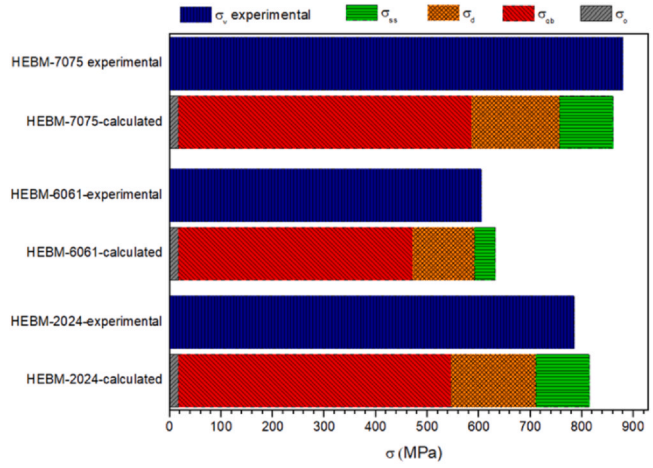

Fig. 10. Experimental yield strength (σ_y, calculated by Tabor's rule) and calculated contributions of base metal (σ_o), grain boundary strengthening (σ_{gb}), dislocation strengthening (σ_d), solid solution strengthening (σ_{ss}) to overall yield strength for HEBM-2024, HEBM-6061, HEBM-7075.

5. Conclusions

The influence of high-energy ball milling on the corrosion and hardness of the AA2024, AA6061 and AA7075 were investigated in this work. Main conclusions can be summarized as follows:

- Homogenous microstructure, free from coarse secondary phases, and significant grain refinement (below 100 nm) were achieved after high-energy ball milling of prealloyed powders.
- High-energy ball milled age hardening alloys exhibited significantly enhanced corrosion resistance as represented by higher pitting and protection potentials, and lower corrosion current densities. High corrosion resistance is attributed mainly to absence of coarse intermetallics, possible incorporation of impurity elements in solid solution, and grain refinement below 100 nm.
- The hardness of the HEBM alloys showed remarkable increase which was attributed to the combined effect of nanocrystalline structure, work hardening and extended solid solubility of the alloying elements in Al matrix. The predominant contribution to the strengthening in the HEBM alloys was by grain refinement which was predicted to between 67% and 75% of total estimated yield strength.
- Hardness and corrosion performance of the age hardening aluminum alloys were enhanced simultaneously by HEBM that can be employed in the production of high strength and corrosion resistant Al alloys.

CRediT authorship contribution statement

F. Ozdemir: Conceptualization, Data curation, Formal analysis, Investigation, Methodology, Validation, Visualization, Writing – original draft, Writing – review & editing. **C.S. Witharamage:** Investigation, Writing – review & editing. **A.A Darwish:** Investigation, Writing – review & editing. **H. Okuyucu**: Writing – review & editing. **R.K. Gupta:** Conceptualization, Data curation, Formal analysis, Supervision, Funding acquisition, Methodology, Validation, Project administration, Resources, Writing – original draft, Writing – review & editing.

Declaration of Competing Interest

The authors declare that they have no known competing financial interests or personal relationships that could have appeared to influence the work reported in this paper.

Acknowledgements

RKG Acknowledges the financial support from the National Science Foundation (NSF-CMMI 1760204) under the direction of Dr. Alexis Lewis. Furkan Ozdemir acknowledges the support by the Scientific and Technological Research Council of Turkey (TUBITAK-BIDEB 2214-A).

References

[1] I.J. Polmear, Light alloys, Light Alloy (2005), https://doi.org/10.1016/B978-0-7506-6371-7.X5000-2
[2] J.R. Davis, Aluminum and Aluminum Alloys, Alloy. Underst. Basics, ASM International, 2001, pp. 351–416, https://doi.org/10.1361/autb2001p351
[3] R.K. Gupta, N.L. Sukiman, M.K. Cavanaugh, B.R.W. Hinton, C.R. Hutchinson, N. Birbilis, Metastable pitting characteristics of aluminium alloys measured using current transients during potentiostatic polarisation, Electrochim. Acta 66 (2012) 245–254, https://doi.org/10.1016/j.electacta.2012.01.090
[4] T. Dorin, N. Stanford, N. Birbilis, R.K. Gupta, Influence of cooling rate on the microstructure and corrosion behavior of Al-Fe alloys, Corros. Sci. 100 (2015) 396–403, https://doi.org/10.1016/j.corsci.2015.08.017
[5] R.K. Gupta, R. Zhang, C.H.J. Davies, N. Birbilis, Theoretical study of the influence of microalloying on sensitization of AA5083 and moderation of sensitization of a model Al-Mg-Mn alloy via Sr additions, Corrosion 70 (2014) 402–413, https://doi.org/10.5006/1117
[6] R.G. Buchheit, A compilation of corrosion potentials reported for intermetallic phases in aluminum alloys, J. Electrochem. Soc. 142 (1995) 3994–3996, https://doi.org/10.1149/1.2048447
[7] N. Birbilis, R.G. Buchheit, Electrochemical characteristics of intermetallic phases in aluminum alloys, Exp. Surv. Discuss. (2005) 140–151, https://doi.org/10.1149/1.1869984
[8] M.K. Cavanaugh, J. Electrochem, C. Soc, M.K. Cavanaugh, J. Li, N. Birbilis, R.G. Buchheit, Electrochemical characterization of intermetallic phases common to aluminum alloys as a function of solution temperature, Electrochem. Charact. Intermet. Phases Common Alum. Alloy. a Funct. Solut. Temp. (2014), https://doi.org/10.1149/2.0361412jes
[9] J. Li, N. Birbilis, R.G. Buchheit, Electrochemical assessment of interfacial characteristics of intermetallic phases present in aluminium alloy 2024-T3, Corros. Sci. 101 (2015) 155–164, https://doi.org/10.1016/j.corsci.2015.09.012
[10] F. Mansfeld, V. Wang, H. Shih, Development of "stainless aluminum", J. Electrochem. Soc. 138 (1991) L74–L75, https://doi.org/10.1149/1.2085513
[11] A.E. Hughes, R. Parvizi, M. Forsyth, Microstructure and corrosion of AA2024, Corros. Rev. 33 (2015) 1–30, https://doi.org/10.1515/corrrev-2014-0039
[12] R.K. Gupta, A. Deschamps, M.K. Cavanaugh, S.P. Lynch, N. Birbilis, Relating the early evolution of microstructure with the electrochemical response and mechanical performance of a Cu-rich and Cu-lean 7xxx aluminum alloy, J. Electrochem. Soc. 159 (2012) C492–C502, https://doi.org/10.1149/2.062211jes
[13] D.Y. Liu, J.F. Li, Y.L. Ma, R.K. Gupta, N. Birbilis, R. Zhang, A closer look at the role of Zn in the microstructure and corrosion of an Al-Cu-Li alloy, Corros. Sci. 145 (2018) 220–231, https://doi.org/10.1016/j.corsci.2018.10.003
[14] P.C. King, I.S. Cole, P.A. Corrigan, A.E. Hughes, T.H. Muster, FIB/SEM study of AA2024 corrosion under a seawater drop: part I, Corros. Sci. 53 (2011) 1086–1096, https://doi.org/10.1016/j.corsci.2010.12.004

[15] N. Birbilis, M.K. Cavanaugh, R.G. Buchheit, Electrochemical behavior and localized corrosion associated with Al7Cu2 Fe particles in aluminum alloy 7075-T651, 48 (2006) 4202–4215. https://doi.org/10.1016/j.corsci.2006.02.007.

[16] G.S. Frankel, Pitting corrosion of metals: a review of the critical factors, J. Electrochem. Soc. 145 (2019) 2186–2198, https://doi.org/10.1149/1.1838615

[17] L.C. Abodi, J.A. Derose, S. Van Damme, A. Demeter, T. Suter, J. Deconinck, Modeling localized aluminum alloy corrosion in chloride solutions under non-equilibrium conditions: steps toward understanding pitting initiation, Electrochim. Acta 63 (2012) 169–178, https://doi.org/10.1016/j.electacta.2011.12.074

[18] Z. Zhao, G.S. Frankel, On the first breakdown in AA7075-T6, 49 (2007) 3064–3088, https://doi.org/10.1016/j.corsci.2007.02.001

[19] K. Nişancıoğlu, Electrochemical behavior of aluminum-base intermetallics containing iron, J. Electrochem. Soc. 137 (2019) 69–77, https://doi.org/10.1149/1.2086441

[20] K.D. Ralston, T.L. Young, R.G. Buchheit, Electrochemical evaluation of constituent intermetallics in aluminum alloy 2024-T3 exposed to aqueous vanadate inhibitors, J. Electrochem. Soc. 156 (2009) C135, https://doi.org/10.1149/1.3076147

[21] G.S. Chen, M. Gao, R.P. Wei, Microconstituent-induced pitting corrosion in aluminum alloy 2024-T3, Corrosion 52 (1996) 8–15, https://doi.org/10.5006/1.3292099

[22] Y.L. Cheng, Z. Zhang, F.H. Cao, J.F. Li, J.Q. Zhang, J.M. Wang, C.N. Cao, A study of the corrosion of aluminum alloy 2024-T3 under thin electrolyte layers, Corros. Sci. 46 (2004) 1649–1667, https://doi.org/10.1016/j.corsci.2003.10.005

[23] A. Staszczyk, J. Sawicki, B. Adamczyk-Cieslak, A study of second-phase precipitates and dispersoid particles in 2024 aluminum alloy after different aging treatments, Mater. (Basel) 12 (2019), https://doi.org/10.3390/ma1224168

[24] E. Sikora, X.J. Wei, B.A. Shaw, Corrosion behavior of nanocrystalline bulk Al-Mg-based alloys, Corrosion 60 (2004) 387–398, https://doi.org/10.5006/1.3287748

[25] J.G. Brunner, N. Birbilis, K.D. Ralston, S. Virtanen, Impact of ultrafine-grained microstructure on the corrosion of aluminium alloy AA2024, Corros. Sci. 57 (2012) 209–214, https://doi.org/10.1016/j.corsci.2011.12.016

[26] N.L. Sukiman, X. Zhou, N. Birbilis, A.E. Hughes, J.M.C. Mol, S.J. Garcia, X. Zhou, G.E. Thompson, Aluminium alloys - new trends in fabrication and applications, Alum. Alloy. - New Trends Fabr. Appl. (2012), https://doi.org/10.5772/3354

[27] B. Sarkar, M. Marek, E.A. Starke, The effect of copper content and heat treatment on the stress corrosion characteristics of Al-6Zn-2Mg-X Cu alloys, Metall. Trans. A, Phys. Metall. Mater. Sci. 12A (1981) 1939–1943, https://doi.org/10.1007/BF02643806

[28] J. Wloka, T. Hack, S. Virtanen, Influence of temper and surface condition on the exfoliation behaviour of high strength Al-Zn-Mg-Cu alloys, Corros. Sci. 49 (2007) 1437–1449, https://doi.org/10.1016/j.corsci.2006.06.033

[29] J. Esquivel, R.K. Gupta, Review—corrosion-resistant metastable Al alloys: an overview of corrosion mechanisms, J. Electrochem. Soc. 167 (2020) 081504, https://doi.org/10.1149/1945-7111/ab8a97

[30] C. Suryanarayana, E. Ivanov, V.V. Boldyrev, The science and technology of mechanical alloying, 306 (2001) 151–158, https://doi.org/10.1016/S0921-5093(00)01465-9

[31] C.C. Koch, The synthesis of non-equilibrium structures by ball-milling, Mater. Sci. Forum 88–90 (1992) 243–262, https://doi.org/10.4028/www.scientific.net/msf.88-90.243

[32] R. Gupta, B. Murthy, N. Birbilis, An Overview of High-energy Ball Milled Nanocrystalline Aluminum Alloys, 1st ed., Springer International Publishing, 2017. https://doi.org/10.1007/978–3-319–57031-0.

[33] J. Esquivel, K.A. Darling, H.A. Murdoch, R.K. Gupta, Corrosion and mechanical properties of Al-5 At. Pct Cr produced by cryomilling and subsequent consolidation at various temperatures, Metall. Mater. Trans. A Phys. Metall. Mater. Sci. 49 (2018) 3058–3065, https://doi.org/10.1007/s11661-018-4620-5

[34] J. Esquivel, R.K. Gupta, Simultaneous improvement of mechanical and corrosion properties of aluminum alloys, Light Met. 151 (2016) 151–156, https://doi.org/10.1002/9781119274780.ch26

[35] R.K. Gupta, D. Fabijanic, T. Dorin, Y. Qiu, J.T. Wang, N. Birbilis, Simultaneous improvement in the strength and corrosion resistance of Al via high-energy ball milling and Cr alloying, JMADE 84 (2015) 270–276, https://doi.org/10.1016/j.matdes.2015.06.120

[36] C.C. Koch, Structural nanocrystalline materials: an overview, (2007) 1403–1414. https://doi.org/10.1007/s10853–006-0609–3.

[37] L. Esteves, C.S. Witharamage, J. Christudasjustus, G. Walunj, S.P.O. Brien, S. Ryu, Corrosion behavior of AA5083 produced by high-energy ball milling, J. Alloy. Compd. 857 (2020) 158268, https://doi.org/10.1016/j.jallcom.2020.158268

[38] E. Kus, Z. Lee, S. Nutt, F. Mansfeld, A comparison of the corrosion behavior of nanocrystalline and conventional Al 5083 samples, Corrosion 62 (2006) 152–161, https://doi.org/10.5006/1.3278260

[39] Y. Minamino, S. Saji, K. Hirao, K. Ogawa, H. Araki, Y. Miyamoto, T. Yamane, Diffusion of copper in nanocrystalline Al-7.8 at%Ti-0.3 at%Fe alloy prepared by mechanical alloying, Mater. Trans. Jim. 37 (1996) 130–137, https://doi.org/10.2320/matertrans1989.37.130

[40] C.C. Koch, J.D. Whittenberger, Mechanical milling/alloying of intermetallics, Intermetallics 4 (1996) 339–355, https://doi.org/10.1016/0966-9795(96)00001-5

[41] K.D. Ralston, N. Birbilis, M.K. Cavanaugh, M. Weyland, B.C. Muddle, R.K.W. Marceau, Role of nanostructure in pitting of Al-Cu-Mg alloys, Electrochim. Acta 55 (2010) 7834–7842, https://doi.org/10.1016/j.electacta.2010.02.001

[42] X. Sauvage, N. Enikeev, R. Valiev, Y. Nasedkina, M. Murashkin, Atomic-scale analysis of the segregation and precipitation mechanisms in a severely deformed Al-Mg alloy, Acta Mater. 72 (2014) 125–136, https://doi.org/10.1016/j.actamat.2014.03.033

[43] M. Zha, H. Zhang, X. Meng, H. Jia, S. Jin, Stabilizing a severely deformed Al–7Mg alloy with a multimodal grain structure via Mg solute segregation, J. Mater. Sci. Technol. 89 (2021) 141–149, https://doi.org/10.1016/j.jmst.2021.01.086

[44] J.L. Searles, P.I. Gouma, R.G. Buchheit, Stress corrosion cracking of sensitized AA5083 (Al-4.5Mg-1.0Mn), Metall. Mater. Trans. A 32A (2001) 2859–2867, https://doi.org/10.1007/s11661-001-1036-3

[45] R.L. Holtz, P.S. Pao, R.A. Bayles, T.M. Longazel, Corrosion-fatigue behavior of aluminum alloy 5083-H131 sensitized at 448K (175 ° C), Metall. Mater. Trans. A. 43 (2012) 2839–2849, https://doi.org/10.1007/s11661-011-0866-x

[46] L. Esteves, J. Christudasjustus, S.P. O'Brien, C.S. Witharamage, A.A. Darwish, G. Walunj, P. Stack, T. Borkar, R.E. Akans, R.K. Gupta, Effect of V content on corrosion behavior of high-energy ball milled AA5083, Corros. Sci. 186 (2021) 109465, https://doi.org/10.1016/j.corsci.2021.109465

[47] H.M. Rietveld, Line profiles of neutron powder-diffraction peaks for structure refinement, Acta Crystallogr. 22 (1967) 151–152, https://doi.org/10.1107/s0365110x67000234

[48] R.A. Young, The rietveld method, 1993.

[49] B.C. Sousa, C. Walde, V.K. Champagne, A.T. Nardi, R.D. Sisson, D.L. Cote, Rapidly solidified gas-atomized aluminum alloys compared with conventionally cast counterparts: implications for cold spray materials consolidation, Coatings 10 (2020) 1–28, https://doi.org/10.3390/coatings10111035

[50] C. Suryanarayana, Mechanical alloying: a novel technique to synthesize advanced materials, Research 2019 (2019), https://doi.org/10.34133/2019/4219812

[51] J.R. Davis, Corrosion of Aluminum and Aluminum Alloys-ASM International, 1999. https://doi.org/DOI:10.1361/caaa1999p001.

[52] L. Lacroix, C. Blanc, N. Pébère, G.E. Thompson, B. Tribollet, V. Vivier, Simulating the galvanic coupling between S-Al2CuMg phase particles and the matrix of 2024 aerospace aluminium alloy, Corros. Sci. 64 (2012) 213–221, https://doi.org/10.1016/j.corsci.2012.07.020

[53] J. Esquivel, R.K. Gupta, Simultaneous Improvement of Mechanical and Corrosion Properties of Aluminum Alloys, in: Light Met. 2016, Springer, Cham, 2016: pp. 151–152. https://doi.org/https://doi.org/10.1007/978–3-319–48251-4_26.

[54] J. Esquivel, H.A. Murdoch, K.A. Darling, R.K. Gupta, Excellent corrosion resistance and hardness in Al alloys by extended solid solubility and nanocrystalline structure, 3831 (2018), https://doi.org/10.1080/21663831.2017.1396262

[55] M.A. Meyers, A. Mishra, D.J. Benson, Mechanical properties of nanocrystalline materials, 51 (2006) 427–556, https://doi.org/10.1016/j.pmatsci.2005.08.003

[56] T. Shanmugasundaram, M. Heilmaier, B.S. Murty, V.S. Sarma, On the Hall – Petch relationship in a nanostructured Al – Cu alloy, 527 (2010) 7821–7825. https://doi.org/10.1016/j.msea.2010.08.070.

[57] C.S. Witharamage, J. Christudasjustus, R.K. Gupta, The effect of milling time and speed on solid solubility, grain size, and hardness of Al-V alloys, J. Mater. Eng. Perform. (2021) 1–15, https://doi.org/10.1007/s11665-021-05663-x

[58] K.A. Darling, A.J. Roberts, L. Armstrong, Influence of Mn solute content on grain size reduction and improved strength in mechanically alloyed Al–Mn alloys, Mater. Sci. Eng. A 589 (2014) 57–65, https://doi.org/10.1016/j.msea.2013.09.047

[59] K. Ma, H. Wen, T. Hu, T.D. Topping, D. Isheim, D.N. Seidman, E.J. Lavernia, J.M. Schoenung, Mechanical behavior and strengthening mechanisms in ultrafine grain precipitation-strengthened aluminum alloy, Acta Mater. 62 (2014) 141–155, https://doi.org/10.1016/j.actamat.2013.09.042

[60] J.E. Bailey, P.B. Hirsch, The dislocation distribution, flow stress, and stored energy in cold-worked polycrystalline silver, Philos. Mag. 5 (1960) 485–497, https://doi.org/10.1080/14786436008238300

[61] R.L. Fleischer, Solution hardening by tetragonal distortions: application to irradiation hardening in F.C.C. crystals, Acta Metall. 10 (1962) 835–842, https://doi.org/10.1016/0001-6160(62)90098-6

[62] J. Esquivel, R.K. Gupta, Influence of the V content on microstructure and hardness of high-energy ball milled nanocrystalline Al-V alloys, J. Alloy. Compd. 760 (2018) 63–70, https://doi.org/10.1016/j.jallcom.2018.05.132

[63] C.C. Koch, Nanostructured materials processing, Properties and Potential Applications Edited, William Andrew Publishing, 2007.

[64] T.D. Shen, C.C. Koch, Formation, solid solution hardening and softening of nanocrystalline solid solutions prepared by mechanical attrition, Acta Mater. 44 (1996) 753–761, https://doi.org/10.1016/1359-6454(95)00178-6

[65] R.G. Buchheit, R.P. Grant, P.F. Hiava, B. Mckenzie, G. Zender, Local dissolution phenomena associated with S phase (Al2CuMg) particles in aluminum alloy 2024-T3, J. Electrochem. Soc. 144 (1997) 2621–2628, https://doi.org/10.1149/1.1837874

[66] N. Birbilis, Y.M. Zhu, S.K. Kairy, M.A. Glenn, J.F. Nie, A.J. Morton, Y. Gonzalez-Garcia, H. Terryn, J.M.C. Mol, A.E. Hughes, A closer look at constituent induced localised corrosion in Al-Cu-Mg alloys, Corros. Sci. 113 (2016) 160–171, https://doi.org/10.1016/j.corsci.2016.10.018

[67] R.K. Gupta, N.L. Sukiman, K.M. Fleming, M.A. Gibson, N. Birbilis, Electrochemical behavior and localized corrosion associated with Mg2Si particles in Al and Mg alloys, ECS Electrochem. Lett. 1 (2012) 2–4, https://doi.org/10.1149/2.002201eel

[68] R.K. Gupta, N. Birbilis, The influence of nanocrystalline structure and processing route on corrosion of stainless steel: A review, Corros. Sci. (2014), https://doi.org/10.1016/j.corsci.2014.11.041

[69] J. Esquivel, R.K. Gupta, Corrosion behavior and hardness of Al-M (M: Mo, Si, Ti, Cr) alloys, Acta Metall. Sin. (Engl. Lett. 30 (2017) 333–341, https://doi.org/10.1007/s40195-017-0550-2

[70] H.P. Godard, The Corrosion of Light Metals, John Wiley & Sons, New York, 1967.

[71] N.D. Nam, V.D. Phung, P.T.P. Thuy, V.A. Dao, S.H. Kim, J.S. Yi, Corrosion behaviours of hot-extruded Al-xMg alloys, 8 (2019) 5246–5253, https://doi.org/10.1016/j.jmrt.2019.08.047

[72] W. Cheng, C.Y. Liu, H.F. Huang, L. Zhang, B. Zhang, L. Shi, High strength and ductility of Al–Si–Mg alloys fabricated by deformation and heat treatment, Mater. Charact. 178 (2021) 111278, https://doi.org/10.1016/j.matchar.2021.111278
[73] M. Zha, H. Zhang, X. Meng, H. Jia, S. Jin, Stabilizing a severely deformed Al–7Mg alloy with a multimodal grain structure via Mg solute segregation, J. Mater. Sci. Technol. 89 (2021) 141–149, https://doi.org/10.1016/j.jmst.2021.01.086
[74] L. Meng, Z. Wang, L. Wang, L. Guo, Z. Guo, Novel and efficient purification of scrap Al-Mg alloys using supergravity technology, Waste Manag 119 (2021) 22–29, https://doi.org/10.1016/j.wasman.2020.09.027
[75] L.X. Bach, D.L. Son, M.T. Phong, L.V. Thang, M.Z. Bian, N.D. Nam, A study on Mg and AlN composite in microstructural and electrochemical characterizations of extruded aluminum alloy, Compos. Part B Eng. 156 (2019) 332–343, https://doi.org/10.1016/j.compositesb.2018.08.139
[76] Y. Geng, I. Panchenko, S. Konovalov, X. Chen, Y. Ivanov, Effect of electron beam energy densities on the surface morphology and tensile property of additively manufactured Al-Mg alloy, Nucl. Instrum. Methods Phys. Res. Sect. B Beam Interact. Mater. At. 498 (2021) 15–22, https://doi.org/10.1016/j.nimb.2021.04.008
[77] J.M. Liang, M.T. Jia, X.Q. Guo, D.L. Zhang, Microstructural evolution and microhardness change of Al–7wt%Si–0.3wt%Mg alloy granules/powder particles during high energy ball milling, Mater. Sci. Eng. A 590 (2014) 307–313, https://doi.org/10.1016/j.msea.2013.10.050
[78] F. Hadef, Synthesis and disordering of B2 TM-Al (TM=Fe, Ni, Co) intermetallic alloys by high energy ball milling: a review, Powder Technol. 311 (2017) 556–578, https://doi.org/10.1016/j.powtec.2017.01.082
[79] N. Qbau, N.D. Nam, N.X. Ca, N.T. Hien, The crack healing effect of scandium in aluminum alloys during laser additive manufacturing, J. Manuf. Process. 50 (2020) 241–246, https://doi.org/10.1016/j.jmapro.2019.12.050
[80] J. Bi, Z. Lei, Y. Chen, X. Chen, Z. Tian, X. Qin, J. Liang, X. Zhang, Effect of Al3(Sc, Zr) and Mg2Si precipitates on microstructure and tensile properties of selective laser melted Al-14.1Mg-0.47Si-0.31Sc-0.17Zr alloy, Intermetallics 123 (2020) 106822, https://doi.org/10.1016/j.intermet.2020.106822
[81] Y. Qi, H. Zhang, X. Nie, Z. Hu, H. Zhu, X. Zeng, A high strength Al–Li alloy produced by laser powder bed fusion: Densification, microstructure, and mechanical properties, Addit. Manuf. 35 (2020) 101346, https://doi.org/10.1016/j.addma.2020.101346
[82] X. Nie, H. Zhang, H. Zhu, Z. Hu, L. Ke, X. Zeng, Effect of Zr content on formability, microstructure and mechanical properties of selective laser melted Zr modified Al-4.24Cu-1.97Mg-0.56Mn alloys, J. Alloy. Compd. 764 (2018) 977–986, https://doi.org/10.1016/j.jallcom.2018.06.032
[83] C. Suryanarayana, Mechanical alloying and milling, Prog. Mater. Sci. 46 (2001) 1–184, https://doi.org/10.1016/S0079-6425(99)00010-9
[84] P. Bhattacharya, P. Bellon, R.S. Averback, S.J. Hales, Nanocrystalline TiAl powders synthesized by high-energy ball milling: effects of milling parameters on yield and contamination, J. Alloy. Compd. 368 (2004) 187–196, https://doi.org/10.1016/j.jallcom.2003.08.079
[85] S. Gates-rector, T. Blanton, The powder diffraction file: a quality materials characterization database, Powder Diffr. 34 (2019) 352–360, https://doi.org/10.1017/S0885715619000812